UNIVERSITY OF LEEDS

This is a repository copy of *Structural transformation of sulfidized zerovalent iron and its impact on long-term reactivity*.

White Rose Research Online URL for this paper:
http://eprints.whiterose.ac.uk/157638/

Version: Accepted Version

Article:
Mangayayam, MC, Perez, JPH, Dideriksen, K et al. (4 more authors) (2019) Structural transformation of sulfidized zerovalent iron and its impact on long-term reactivity. Environmental Science: Nano, 6 (11). pp. 3422-3430. ISSN 2051-8153

https://doi.org/10.1039/c9en00876d

© The Royal Society of Chemistry 2019. This is an author produced version of an article published in Environmental Science: Nano. Uploaded in accordance with the publisher's self-archiving policy.

Reuse
Items deposited in White Rose Research Online are protected by copyright, with all rights reserved unless indicated otherwise. They may be downloaded and/or printed for private study, or other acts as permitted by national copyright laws. The publisher or other rights holders may allow further reproduction and re-use of the full text version. This is indicated by the licence information on the White Rose Research Online record for the item.

Takedown
If you consider content in White Rose Research Online to be in breach of UK law, please notify us by emailing eprints@whiterose.ac.uk including the URL of the record and the reason for the withdrawal request.

White Rose university consortium
Universities of Leeds, Sheffield & York

eprints@whiterose.ac.uk
https://eprints.whiterose.ac.uk/

Structural transformation of sulfidized zerovalent iron and its impact on long-term reactivity[†]

Marco C. Mangayayam[a*], Jeffrey Paulo H. Perez[b,c], Knud Dideriksen[d], Helen Freeman[b,e], Nicolas Bovet[a,f], Liane G. Benning[b,c], Dominique J. Tobler[a*]

[a]*Nano-Science Center, Department of Chemistry, University of Copenhagen, Universitetsparken 5, 2100 Copenhagen, Denmark*

[b]*GFZ German Research Center for Geosciences, Telegrafenberg, 14473 Potsdam, Germany*

[c] *Department of Earth Sciences, Free University of Berlin, 12249 Berlin, Germany*

[d]*Geological Survey of Denmark & Greenland (GEUS), Øster Voldgade 10, 1350 Copenhagen, Denmark*

[e]*School of Chemical and Process Engineering, University of Leeds, Leeds, LS2 9JT, United Kingdom*

[f]*Danish Hydrocarbon Research and Technology Centre (DHRTC), Danish Technical University, Kongens Lyngby, Denmark*

**Corresponding authors: mc.marco@chem.ku.dk and dominique.tobler@chem.ku.dk*

[†]*Electronic supplementary information (ESI) available.*

Environmental significance

Sulfidized nanoscale zerovalent iron (S-nZVI) has been shown to efficiently degrade contaminants for *in-situ* groundwater remediation applications. Yet, less is known about the S-nZVI core-shell structure and how this heterogenous architecture transforms once exposed to groundwater conditions. This is important as it gives insights into the stability of S-nZVI under relevant environmental settings thereby elucidating the key surface processes that permit S-nZVI to sustain reactivity over prolonged periods.

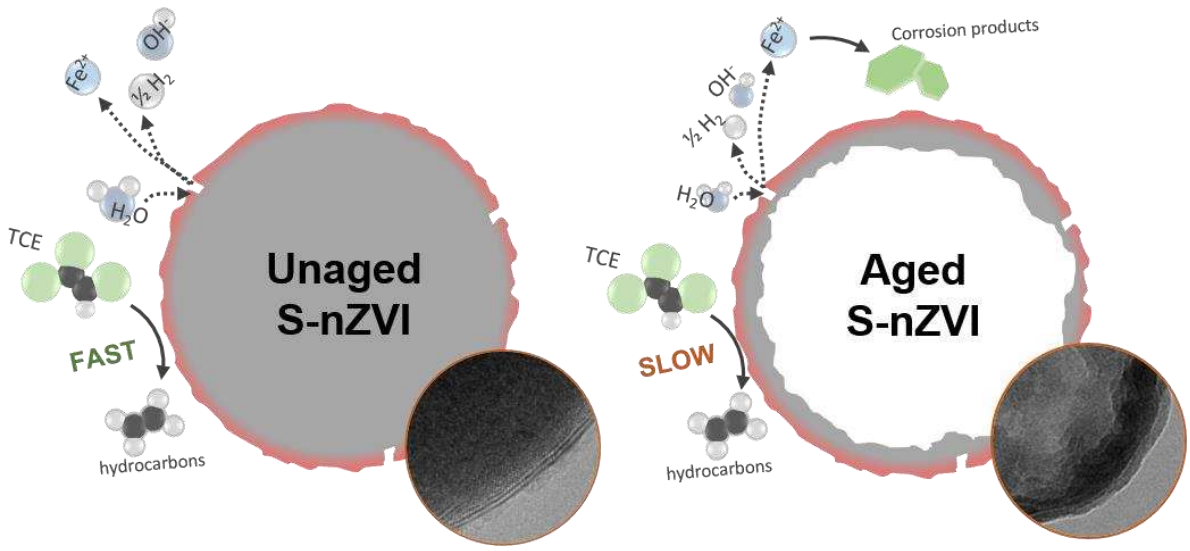

Table of Contents Art

Abstract

Sulfidized nanoscale zerovalent iron (S-nZVI), synthesized via two-step using Na_2S, is an emerging *in-situ* material for groundwater remediation, composed of a metallic iron core and iron sulfide shell. The shell efficiently transfers electrons from the core to its surface for contaminant reduction, while simultaneously protecting the core from anoxic corrosion. However, what controls the S-nZVI longevity is poorly understood. In this study, we characterized at high resolution the structure of S-nZVI and assessed its reactivity with trichloroethene (TCE) with increasing aging. Our data of freshly synthesized material show that the S-nZVI shell primarily consists of ~5-nm-thick nanocrystalline mackinawite (FeS_m) with structural imperfections and heterogeneous crystal orientations. As S-nZVI was aged in anoxic artificial groundwater for up to 180 days, the shell remained mostly intact, while the iron core significantly corroded, resulting in hollow particle structures. We interpret that FeS_m defects caused the deterioration of the core. Between 0 and 120 days of aging, rate constants for TCE reduction decreased by only ~41%. This shows that FeS_m remained accessible for TCE reduction; but as the core became depleted, the reduction rate decreased. Re-spiking experiments with TCE oxidized ~1/4 of the core while the FeS_m structure was unaffected. This indicates that the FeS_m does not oxidize during TCE reduction, but merely transfers the electron from the core. Overall, these results

demonstrate that S-nZVI is able to sustain its reactivity over extended periods due to the persistence of FeS_m against oxidation, while its defects control the extent of core corrosion.

Keywords: sulfidation, mackinawite, ZVI, remediation, groundwater, nanoparticles, corrosion

1. Introduction

A large number of studies show that sulfidation of nanoscale zerovalent iron (S-nZVI) with sodium sulfide (Na_2S) enhances the removal of a range of groundwater contaminants compared to non-sulfidized nanoscale ZVI (nZVI).[1–5] This enhanced reactivity depends on the used S/Fe ratio during sulfidation, which seems to control the thickness and structure of the iron sulfide shell that forms around the metallic iron (Fe^0) core.[3,4] The shell is suggested to have conductive properties, allowing for electron transfer from the Fe^0 core to the S-nZVI surface.[1,3,4] Synergistically, the shell limits oxidation of the Fe^0 core by water (i.e., anaerobic corrosion), thus decreasing loss of electrons compared to nZVI,[6] which in turn gives S-nZVI higher longevity in groundwater settings.

Despite the extensive literature on S-nZVI, surprisingly, we still know very little about the nature of this iron sulfide shell and how it enables such efficient contaminant reduction, particularly after prolonged exposure to anoxic waters and contaminants. Some initial characterization using high-resolution X-ray diffraction (XRD) has shown that the shell consists of poorly crystalline mackinawite (FeS_m) with an expanded basal plane spacing.[2] The chemical composition of this FeS_m shell structure has been confirmed by X-ray photoelectron spectroscopy (XPS) and energy-dispersive X-ray spectroscopy (EDXS),[4,7] and its low reactivity with water has been demonstrated by low H_2 formation rates.[4,6] In terms of S-nZVI longevity, Fan et al.[6] observed that when S-nZVI was aged for 21 days in deoxygenated, deionized water, its reactivity with indigo carmine decreased by only ~5-10%, with little indication of Fe^0 corrosion during these 21 days. When S-nZVI is aged for longer time spans, however, the Fe^0 core becomes substantially corroded and S-nZVI reactivity decreases more profoundly as

65 demonstrated by Xu et al.[5] Specifically, they reported a ~45% decrease in Fe^0 content and ~50 %
66 decrease in trichloroethene reduction rate for S-nZVI aged for 60 days in deoxygenated, deionized
67 water. Similarly, Fan et al.[2] showed that S-nZVI aged with pertechnetate (TcO_4^-) for 2 months led to
68 hollow S-nZVI particles with depleted Fe cores. To compare, nZVI, the current state of the art reductant
69 particle in groundwater remediation, exhibited substantial corrosion and complete loss in TCE
70 reactivity after only 1-2 weeks of aging in anoxic waters.[5,8,9] While these studies clearly demonstrated
71 the higher longevity of S-nZVI compared to nZVI upon exposure to anoxic waters, little has been done
72 to assess the progressive structural changes of S-nZVI upon aging. As such we have limited insight into
73 Fe^0 and/or FeS_m corrosion processes on S-nZVI surfaces nor do we know the parameters that
74 accelerate or limit them. This understanding is critical to make accurate predictions about S-nZVI
75 corrosion behavior and ultimately its long-term fate in groundwater settings.

76 To close this gap, we have performed high-resolution structural and compositional characterization of
77 freshly synthesized S-nZVI and S-nZVI aged in anoxic artificial groundwater for up to 180 days using
78 high resolution electron microscopy, high energy X-ray scattering and spectroscopic techniques. These
79 observations were complemented with reactivity data, by determining TCE reduction rates for
80 progressively aged S-nZVI. In addition, S-nZVI structural and reactivity changes were further assessed
81 in TCE re-spiking experiments, to mimic S-nZVI fate in a contaminated subsurface. Finally, these data
82 were used to build a conceptual model of S-nZVI redox sites and their stability and fate upon exposure
83 to groundwaters, in order to predict S-nZVI performance in field scale applications.

84

85 **2. Materials and Methods**

86 All syntheses, aging, and sample preparations for characterization were done inside an anoxic, vinyl-
87 walled glove box (95% N_2/5%H_2; Coy laboratories) using reagent grade chemicals (supplementary
88 information, SI, Text S1) and deoxygenated, deionized water (MilliQ, resistivity > 18 Ωcm).

89

90 *2.1 S-nZVI Synthesis*

91 Sulfidized nanoscale zero valent iron (S-nZVI) synthesis was based on a modified procedure from
92 Rajajayavel et al.[4] in which nZVI was produced by reduction of $FeCl_2$ using sodium borohydride. The,
93 nZVI was reacted with a Na_2S solution in acetate-buffer (pH ~6.0±0.1) for 3 hours. The resulting S-nZVI
94 particles were washed thrice with 96% ethanol, vacuum filtered, and then used for characterization,
95 aging, and reactivity studies. Additional synthesis details are given in SI, Text S2.

96

97 *2.2 S-nZVI aging experiments*

98 The freshly synthesized S-nZVI particles were aged for up to 180 days (mass loading of 1 g L^{-1}) in 150
99 mL anoxic artificial groundwater (water composition given in SI, Table S1), prepared using a previously
100 established procedure.[10] The reactors were capped with Viton rubber stoppers and kept inside the
101 anoxic glovebox without shaking throughout the aging process. Between 0 and 180 days, aliquots were
102 removed to isolate the aged particles for structural and compositional characterization (SI, Text S3).
103 To assess the reactivity of these progressively aged S-nZVI, identical S-nZVI groundwater aging reactors
104 were set up as explained above. After specific aging times, a reactor was sacrificed and spiked with
105 110 µM TCE to initiate the reaction. Once the TCE was added, the decrease in TCE concentration was
106 monitored over the following 50 hours using gas chromatography – mass spectroscopy (GC-MS) to
107 derive reaction rates. Specific details are given in SI, Text S4, including set-up of controls and GC-MS
108 measurement procedures.

109 In a separate reactor, freshly synthesized S-nZVI (mass loading of 1 g L^{-1} in 150 mL anoxic artificial
110 groundwater) was exposed to 7 sequential 110 µM TCE amendments over a total of 11 days. Re-
111 spiking of TCE occurred once the former injected TCE concentration was reduced to < 5%. TCE removal

was regularly monitored using GC-MS and rates for each re-spike were derived using identical protocols as explained for TCE reactivity experiments (SI, Text S4).

2.3 S-nZVI characterization

The bulk structure of S-nZVI was determined with synchrotron-based X-ray diffraction (XRD) and pair distribution function (PDF) analyses at beamline 11-ID-B (58 keV, λ = 0.2114 Å) at the Advanced Photon Source, Argonne National Laboratory (USA).[8,11] The S-nZVI surface composition was determined with X-ray photoelectron spectroscopy (XPS) using a Kratos Axis Ultra^{DLD} with a monochromated Al Kα X-ray source (hv = 1486.6 eV, power = 150 W), pass energy of 20 eV and analysis spot size of about 700 µm x 300 µm. The size, morphology, and spatial chemical composition of S-nZVI were characterized by transmission electron microscopy (TEM) and scanning electron microscopy (SEM). The TEM images, selected area diffraction patterns (SAED), as well as electron dispersive X-ray (EDX) spectra and elemental maps were acquired using an FEI tecnai G20 F20 X-Twin FEG S/TEM operated at 200 kV and equipped with a Gatan imaging filter (GIF) Tridiem^{TM}, a Ficshione high angle annular dark field (HAADF) detector and an EDAX X-ray analyzer. SEM images were acquired using FEI Quanta 3D FEG SEM at 7 kV and 8.7 pA using a secondary electron detector. Full details of sample handling, data measurement and analyses are given in SI, Text S3.

3. Results and Discussions

3.1 Structure of initial S-nZVI

In synchrotron XRD patterns (I(Q)), unaged S-nZVI exhibits broad peaks at 3.09 Å^{-1} (2.03 Å) and 5.35 Å^{-1} (1.17 Å), which correspond to the (110) and (211) planes of nanocrystalline α-Fe (i.e., Fe^0 core, Figure 1a).[12] An additional smaller peak exists at ~1.19 Å^{-1} (5.28 Å), matching the (001) reflection of mackinawite (FeS_m) but with a ~5% expanded basal plane spacing, relative to a nanocrystalline

136 mackinawite (Figure 1a),[13,14] as previously observed for these materials using XRD.[2] The PDFs were
137 extracted from the I(Q) to determine the interatomic distances (Figure 1b). Overall, the PDF of S-nZVI
138 resembles the pattern for the non-sulfidized ZVI, where the peaks for the first (r = 2.48 Å) and second
139 (r = 2.56 Å) shell Fe^0-Fe^0 are broadened and cannot be readily distinguished,[8] indicative of local
140 disorder in the structure of the Fe^0 core. Oscillations decay quickly with increasing r-value, showing
141 that long range order was limited. To isolate the PDF of the shell, a differential PDF (d-PDF) was
142 extracted by subtracting the PDF of nZVI from that of S-nZVI (Figure 1c).[8,15,16] The d-PDF exhibits peaks
143 at positions matching a synthetic mackinawite (Figure 1c).[17–19] This implies that while its interlayer was
144 expanded slightly (i.e., ~5% increased basal spacing), its local atomic configuration within the layers
145 maintained the mackinawite-like structure.[20,21]

146

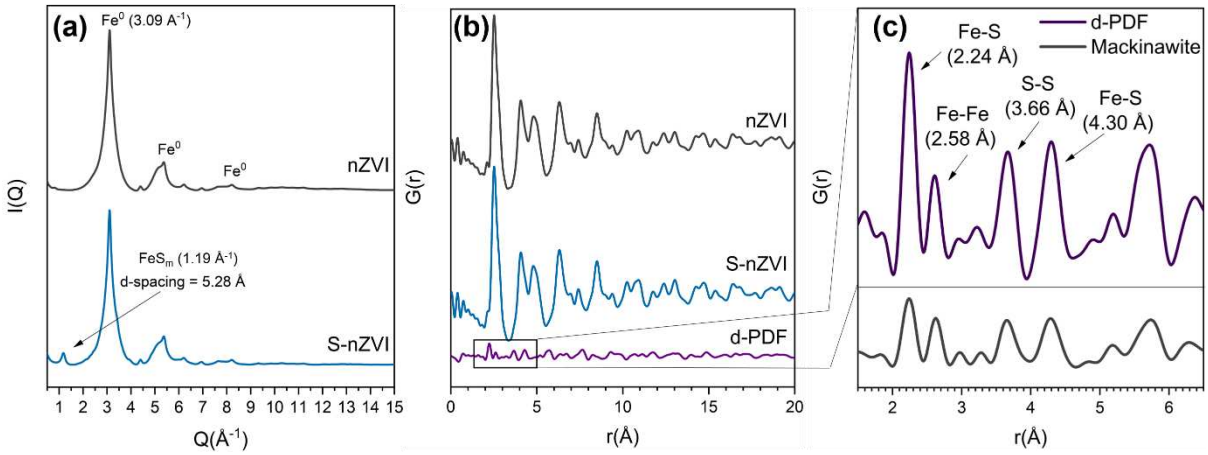

147

148 Figure 1. (a) I(Q) and (b) PDFs of sulfidized and non-sulfidized zero-valent iron (S-nZVI and nZVI). (c) d-
149 PDF (= $PDF_{S\text{-}nZVI} - PDF_{nZVI}$) showing pair correlations that match a mackinawite-like phase. The PDF of
150 synthetic pure mackinawite is given as reference.

151

152 TEM images of freshly prepared S-nZVI show spherical particles of high contrast about 50-150 nm in
153 size (Figure 2a). The majority of the particles were coated by a shell of less electron dense material
154 about ~5 nm thick (Figure 2b). EDX maps reveal that the shell material contained both Fe and S (Figure

155 2c) and selected area electron diffraction (SAED) only shows reflections for Fe^0 and FeS_m (SI, Figure
156 S2). At high resolution, parts of the shell show lattice fringes with d-spacings of 5.4 ± 0.2 Å (Figure 2d),
157 similar to the expanded (001) FeS_m reflection in I(Q) (Figure 1a).[22] Moreover, the FeS_m crystals were
158 often curving around the Fe^0 core, and oriented to expose its (001) surface to the bulk solution (SI,
159 Figure S3). Other parts of the shell exhibit FeS_m layers with no apparent structural coherence (SI, Figure
160 S3), an indication of defects in the shell. In addition, the shell in places showed a sheet-like morphology
161 and different crystal orientations (Figure 2e), with a d-spacing value of 3.1±0.1 Å appearing in 2D fast
162 Fourier transforms (Figure 2e, inset). This distance is consistent with FeS_m (011) plane,[23] which may
163 indicate that the observed area are FeS_m sheets emplaced perpendicularly with respect to the electron
164 beam. This variability in crystal orientation along with the observed lattice mismatches implied a
165 degree of heterogeneity in the FeS_m shell architecture.

166 In summary, our characterization reveals that the shell of freshly synthesized S-nZVI was composed of
167 a ~5 nm thick FeS_m layer with expanded interlayers surrounding the Fe^0 core. While the FeS_m shell
168 surface dominantly exposes its (001) surface, parts of the FeS_m shell exhibit structural discontinuities,
169 caused by defects and variability in crystal orientations. This shell architecture is distinct from that of
170 sulfidized ZVI particles produced via the one-pot dithionite synthesis, which was observed to be
171 substantially thicker, more flakey and dominated by amorphous ferrous hydroxide (white rust) with
172 some amorphous FeS close to the Fe^0 core interface.[3,8,24]

173

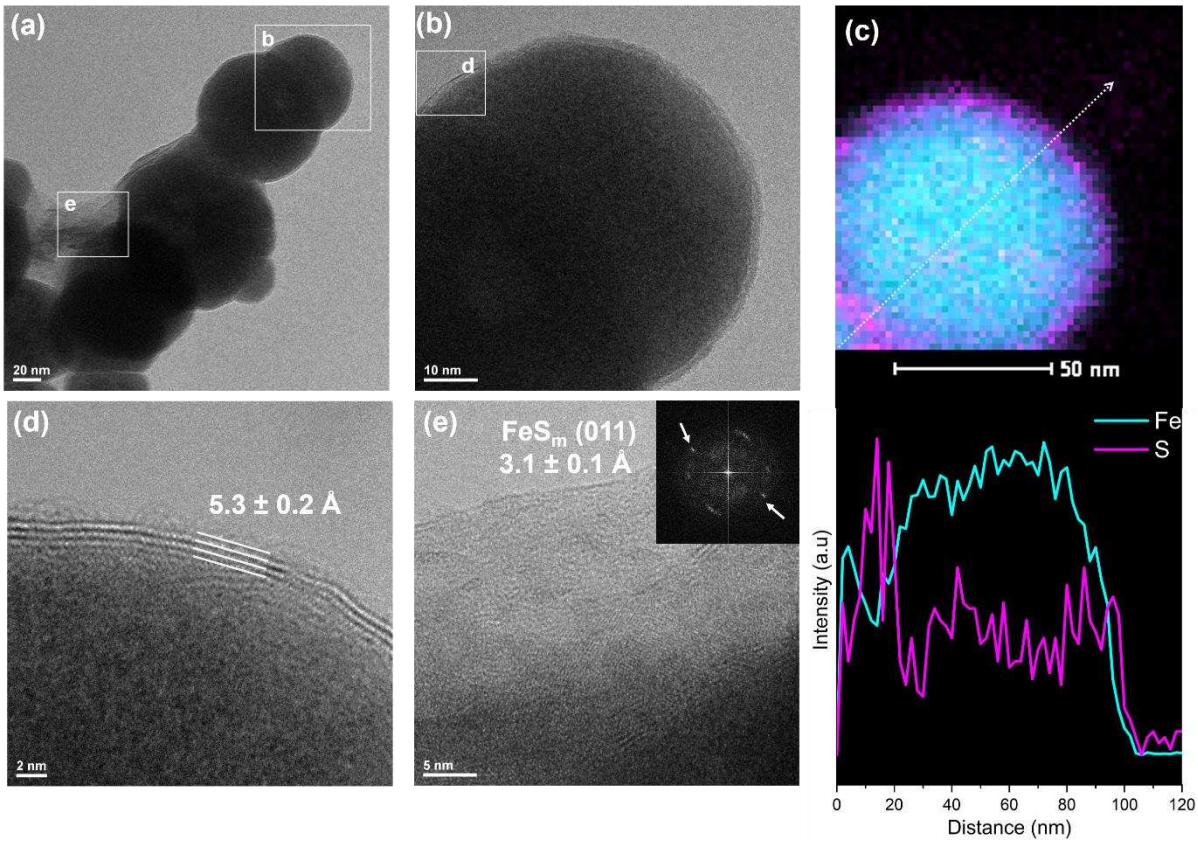

Figure 2. TEM and EDX analyses of freshly synthesized S-nZVI. (a) S-nZVI aggregate showing particle size distribution and areas where high-resolution analyses were performed. b) S-nZVI particle showing electron dense core surrounded by ~5 nm thick, less electron dense shells. (c) EDX map (top) and line intensity profile (bottom) normalized to unity of an isolated particle confirm the Fe-rich core, surrounded by a shell enriched in both sulfur and iron.[7,24] (d) Lattice fringes in the shells have d-spacings consistent with the I(Q) peak for FeS (001).[22] (e) Isolated area showing FeS_m crystal orientation leading to lattice fringes with d-spacing consistent with (011).

3.2 S-nZVI aged in anoxic artificial groundwater

The continued exposure of S-nZVI to anoxic artificial groundwater led to progressive structural and compositional changes as shown by XRD, PDF and XPS (Figure 3a-d). In XRD patterns, peaks from the Fe^0 core decrease in intensity with material age while peaks associated with carbonate green rust (GR_{CO3}) and white rust (WR) increase (Figure 3a). Consistent with XRD, PDFs show a progressive

188 increase in $Fe^{II/III}$-O (~2.11 Å) and Fe^{II}-$Fe^{II/III}$ (~3.19 Å) distances stemming from the formation of
189 corrosion products (i.e., GR_{CO3}, WR, Figure 3b), while peak intensity for Fe^0-Fe^0 distance decrease (e.g.,
190 2.53 Å, Figure 3b). Using these relative changes in PDF peak intensities, we have approximated the
191 decrease in Fe^0 core material with aging (details of results in SI, Table S3 and Figure S4; methods in
192 Text S3). Over the first 10 days of aging, no significant changes in Fe^0-Fe^0 PDF peak heights are
193 observed, suggesting that Fe^0 oxidation (i.e., corrosion) was negligible. From day 10 to 60, the Fe^0-Fe^0
194 peak progressively decreased, indicating the decrease in molar fraction of Fe^0 to about 50% of its initial
195 amount due to corrosion from aging. From day 60 to 120, only slight additional corrosion occurred. In
196 comparison, corrosion of nZVI started instantaneously and occurred substantially faster, with almost
197 80% of the Fe^0 oxidized after 60 days (SI, Figure S5, S6).

198 These progressive structural changes are also evident in the observed surface compositional changes
199 based on our XPS data. The Fe $2p_{3/2}$ spectra (Figure 3c) show a progressive decrease in Fe^{2+}-S/Fe^0
200 species (peak at binding energy, BE = ~706 eV), while Fe^{2+}-O species (broad peak at BE = ~710 eV)
201 increase with aging (SI, Table S4). Similarly, peaks for S^{2-} species (BE = ~161 eV) in the S 2p spectra
202 gradually decrease (Figure 3d), while the intensity for SO_4^{2-} species (BE = ~169 eV) progressively
203 increases (SI, Table S5). Peak deconvolution of the S 2p spectra shows that the amount of transient
204 sulfur species (i.e., S_n^{2-}, S(0), S_2^{2-}) was fairly constant with aging time (i.e., consistently below 12% of
205 total surface sulfur, SI, Table S5). This suggests that transient sulfur species did not evolve from S^{2-}
206 oxidation by aging. These species may have likely formed from oxidation due to quick exposure (< 1
207 minute) of the samples to ambient atmosphere during transfer to the XPS sample entry chamber.[25]
208 Given that no systematic changes in transient sulfur species were measured, the observed increase in
209 SO_4^{2-} is most likely linked to SO_4^{2} adsorption from bulk solution (0.25 mM SO_4^{2-} initially present) by the
210 corrosion products that progressively formed upon aging (SI, Table S6).[26] Similarly, the observed
211 progressive decrease in S^{2-} peak intensity is caused by the gradual increase in voluminous corrosion
212 products, which systematically decreased the amount of S-nZVI that were detected within the area of
213 analysis (i.e., S species; Table S6).

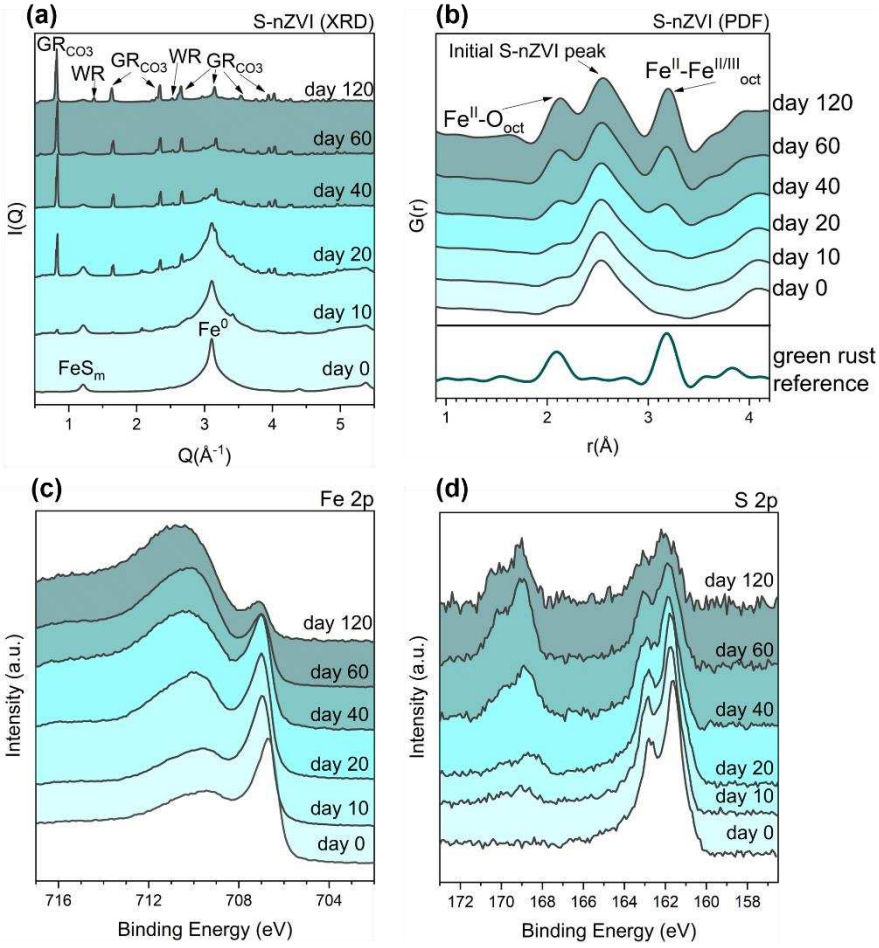

Figure 3. (a) XRD patterns of S-nZVI aged in artificial groundwater showing the gradual formation of secondary carbonate green rust (GR_{CO3}) and white rust (WR). (b) PDF patterns show changes in the local coordination of S-nZVI upon aging for 120 days. A PDF of green rust is also shown to ease identification of the developing $Fe^{II/III}$-O and Fe^{II}-$Fe^{II/III}$ distances. XPS spectra of (c) Fe $2p_{3/2}$ and (d) S 2p, showing changes in surface Fe and S species as a function of aging time.

It is predicted that with continued S-nZVI aging, Fe^0 corrosion processes would certainly proceed but at much lower rates seeing that little structural changes occurred between 60 and 120 days. To visualize the effects of continued aging, TEM imaging and EDX elemental mapping were performed on S-nZVI particles after 180 days of aging (Figure 4). Compared to the initial material (Figure 2a), the

aged particles show “hollow” cores, seemingly devoid of electron dense material (i.e., little contrast remained), while the shell (i.e., interface) appears intact with some parts having laminar or sheet-like structures (Figure 4a, b). EDX mapping and normalized line intensity profiles of the “hollow” particles show low Fe signals for the core but high Fe and S signals for the shell (Figure 4c). At higher resolution, particle cores exhibit variations in contrast (Figure 4b, d), suggesting that material loss occurred heterogeneously within a single particle, and also differed among particles. Closer inspection of the shell show that the (001) mackinawite-like plane are still present, even after 180 days aging (d = 5.2±0.2 Å, Figure 4e). Similarly, the SAED pattern of the aged particles exhibit patterns that may be indexed to a mackinawite-like phase with extended d-spacings (SI, Figure S7). In agreement with XRD, PDF and XPS, both SEM and TEM analyses suggest that GR_{CO3} is the main corrosion product (Figure 5). In addition, SEM and TEM images show that GR_{CO3} formed micron-sized, hexagonal platelets that seem spatially separated from S-nZVI particles.

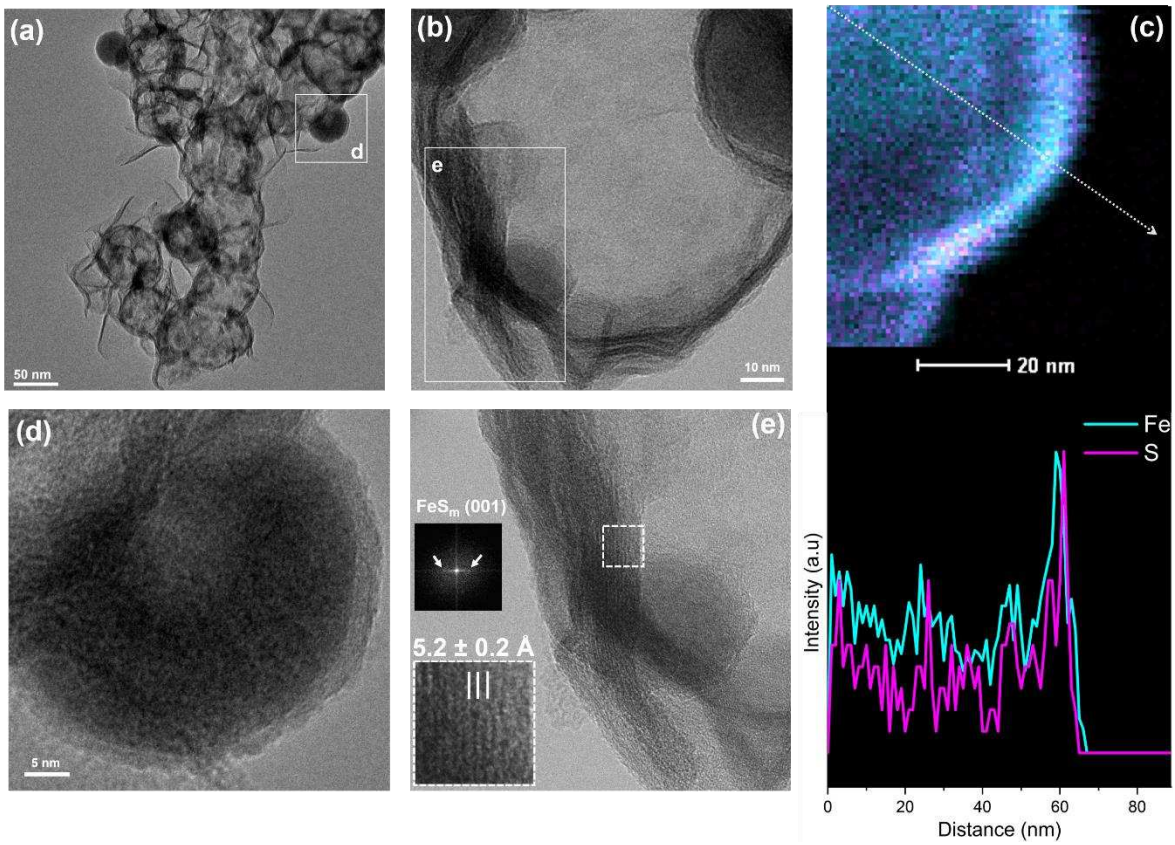

Figure 4. TEM and EDX analyses of S-nZVI particles that were aged for 180 days in anoxic artificial groundwater. (a) An aggregate of aged S-nZVI particles. (b) A particle showing a "hollow" core surrounded by an intact mackinawite-like shell. (c) EDX map (top) and the line intensity profiles of Fe and S normalized to unity (bottom). (d) High resolution TEM image of a particle with substantial core material and a ~5 nm shell with fringes. (e) High resolution TEM image of an isolated shell structure showing lattice fringes (d = 5.2±0.2, inset) that match the basal-spacing of the (001) FeS_m features observed for unaged S-nZVI (Figure 2d). This is further confirmed by the FFT of the same image.

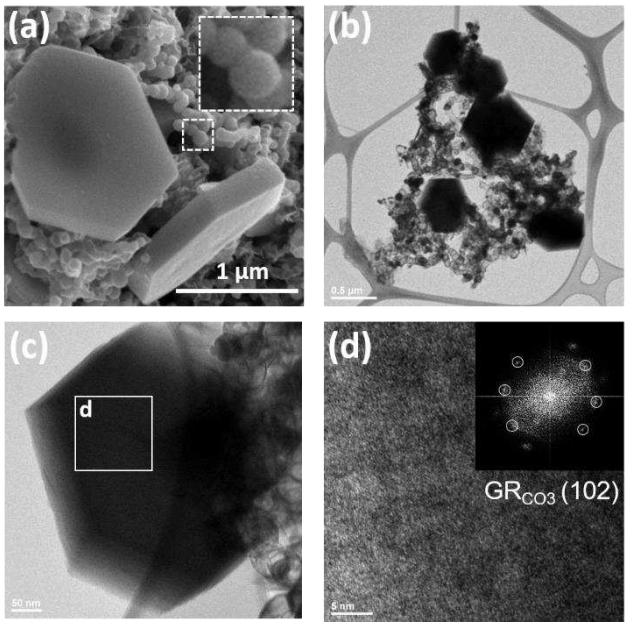

Figure 5. SEM and TEM analyses of 180 day aged S-nZVI. (a) SEM image shows large, hexagonal crystal platelets characteristic of carbonate green rust (GR_{CO3}) and spherical S-nZVI particles (inset). (b) Low resolution TEM image of GR_{CO3} platelets surrounded by aged S-nZVI (c) HR-TEM of GR_{CO3} showing area where (d) FFT image was obtained. The FFT pattern matches (102) plane of GR_{CO3} with d-spacing = 2.6 Å.[27]

255 In terms of TCE reactivity, all aged S-nZVI fully reduced the initially added 110 µM TCE within 50 hours
256 (SI, Figure S8), but aging time affected the reduction rate. Within the first 10 days of aging, the rate
257 constant (k_{obs}) minimally changed (~0.17 h^{-1}, SI, Table S7). It then decreased from 0.16 to 0.12 h^{-1} for
258 S-nZVI aged from 20 to 60 days, before stabilizing around a value of 0.10 h^{-1} after 120 days of aging.
259 Despite this decline in S-nZVI reduction rate over 4 months, the material is still highly reactive;
260 particularly when comparing to nZVI aging results in our previous study, where TCE reduction became
261 negligible after 7 days aging of nZVI under identical conditions.[8]

262

263 *3.3 S-nZVI aged by re-spiking with TCE*

264 Over 11 days, 1 gL^{-1} S-nZVI suspended in the groundwater matrix was exposed to 7 TCE re-spikes (each
265 110 µM). The TCE was continuously and rapidly degraded by S-nZVI, with rates progressively
266 decreasing with each re-spike (SI, Figure S9, Table S8). XRD and PDF characterization of the solids at
267 the end of the 7th TCE re-spike showed the presence of GR_{CO3} and magnetite (M) as corrosion products
268 (SI, Figure S10, S12), and a clear depletion in Fe core material by ~21% (based on PDF peak analyses),
269 which matched well with the theoretical electron consumption of ~25% (based on added S-nZVI and
270 TCE and assuming an average consumption of 6 electrons to fully reduce one TCE molecule).[28] These
271 data further show that the FeS_m shell was still apparent (i.e., peak at 1.19 A^{-1}, SI, Figure S10) and that
272 no other iron sulfide phases could be detected. Overall, the observed changes in structure and
273 reactivity upon TCE re-spiking are very similar to aging in anoxic groundwater alone (section 3.2).
274 However, these changes occurred at different rates. For the groundwater aging experiments, little if
275 any structural changes were observed over the first 10 days; whereas in a similar time span, changes
276 were observed in the re-spiking experiments, indicating that TCE was the main oxidant and responsible
277 for Fe^0 oxidation in the re-spiking experiment (Figure S11). Lastly, despite the presence of a stronger
278 oxidant in these experiments (i.e., TCE), synchrotron-based XRD indicates that the shell structure was
279 unaffected, with no signs of shell oxidation and/or re-crystallization.

280

281 *3.4 Conceptual model of S-nZVI redox sites and their fate with aging*

282 Overall, our experiments in simulated anoxic groundwater showed that:

283 i) Core corrosion of S-nZVI occurred slower in the absence of a strong oxidant (e.g., TCE, Figure 3b, S4)
284 in comparison to reactions where TCE is continuously present (Figure S11), allowing it to conserve its
285 electron pool (i.e., reactivity) for prolonged periods. In comparison, nZVI exhibited rapid core
286 corrosion by anoxic artificial groundwater (Figure S6), as well as almost complete reactivity loss after
287 only 7 days, as shown in our previous study.[8]

288 ii) There is no indication that the FeS_m shell underwent re-crystallization and/or oxidation, whether
289 exposed to TCE or anoxic artificial groundwater. This is in contrast to previous S-nZVI aging studies,
290 which argued that the instability of the shell controls reactivity loss.[6] Our results, however, are more
291 consistent with another study on pure mackinawite systems, where the authors demonstrated the
292 stability of the mackinawite structure even after 106 days of aging in a highly reducing and alkaline
293 aqueous environment.[29]

294 iii) The observed decrease in TCE k_{obs} with aging time seemed to follow the depletion in the Fe^0 core
295 volume (Figure 6), suggesting that the cause of the decrease in TCE reactivity likely stems from the
296 loss in Fe^0. Previous studies have proposed that shell re-crystallization and precipitation of corrosion
297 products on the surface cause the decrease in k_{obs}.[6,30,31] Our characterization showed that the
298 corrosion products formed external to S-nZVI particles aged in anoxic artificial groundwater (Figure 5).
299 These observations may indicate that k_{obs} values are likely also influenced by the Fe^0 core content and
300 the specific corrosion pathways, which in turn control type and location of secondary mineral
301 formation.

302

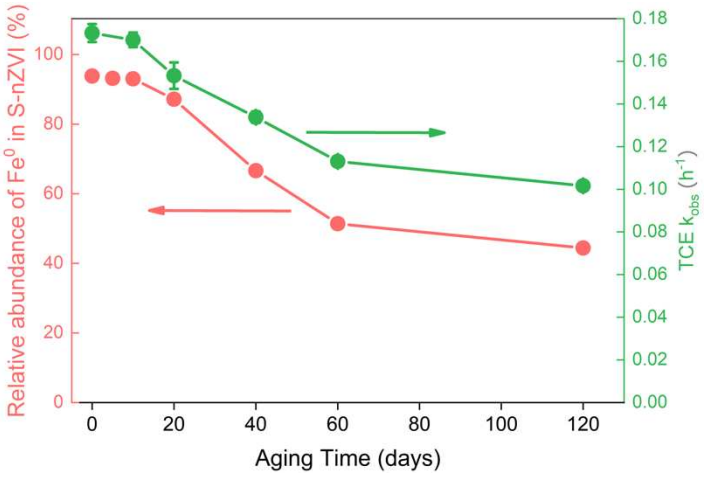

Figure 6. The decrease in S-nZVI Fe^0 content (in red) and TCE reduction rate constant, k_{obs}, (in green) as a function of aging time. The error bars represent the standard error of the fitted k_{obs} from linear regression calculations (Fig. S8).

To create a conceptual model of the active redox sites on S-nZVI surfaces that is consistent with our observations, let us first consider the case of aging in groundwater (without TCE present). The formation of hollow S-nZVI particles, with depleted Fe^0 cores and intact shell structures, has been observed once before for S-nZVI (two-step synthesis, Na_2S precursor) when it was reacted with pertechnetate (TcO_4^-) for 2 months.[2] The authors linked this transformation to nanoscale Kirkendall effect based on similarities to structures observed for Cu^0 nanoparticles transformed under sulfate reducing conditions.[2,32] However, such a process seems unlikely in our aging experiments because solid state diffusion via Kirkendall effect typically requires elevated temperatures since the reaction is kinetically limited at ambient temperatures.[33] If not by solid state diffusion, the generated Fe^{2+} must have been able to transfer into bulk solution by some other mechanisms. This is because we do not see any clear evidence for localized corrosion product formation inside these aged "hollow" S-nZVI particles. Close examination of the FeS_m shell showed numerous shell defects and plane boundaries, which indicate that the shell exhibits "weak" points, where diffusion processes could occur more easily, i.e., allowing for water and ions to access the Fe^0 core. Indeed, such a scenario is supported by

322 our groundwater aging results, where little corrosion occurred in the first 10 days. However, after
323 prolonged incubation (~10-20 days), which gave time for local dissolution and/or diffusion processes
324 at these weak points, water started to interact with Fe^0 sites, leading to continued Fe^0 oxidation (i.e.,
325 core depletion) from then onwards. In such a scenario, it is expected however, that these weak points
326 should be quickly passivated by surface precipitates due to the concomitant occurrence of anodic (Eq.
327 1) and cathodic reaction (Eq. 2) that favors $Fe(OH)_2$ (white rust) formation (Eq. 3):

328 $$Fe^0 \rightarrow Fe^{2+} + 2e^- \ (anodic\ sites) \quad (1)$$

329 $$2e^- + 2H_2O \ \rightarrow \uparrow H_2 + 2OH^- \ (cathodic\ sites) \quad (2)$$

330 $$Fe^0 + 2H_2O \rightarrow Fe(OH)_2 \downarrow + H_2(g) \uparrow \quad (3)$$

331 There is no clear indication of surface passivation in SEM and TEM images and we see continued high
332 TCE reactivity by the aged S-nZVI. Thus, for continued Fe^0 core depletion without substantial internal
333 mineral formation, we propose that the anodic and cathodic sites must have been locally separated
334 on the S-nZVI surface. The separation allows for localized acidification and dissolution at anodic sites;
335 and localized basic conditions and H_2 evolution at the cathodic sites. At the anodic sites, the
336 acidification caused for the eventual opening of the shell weak points, which led to more favorable
337 Fe^{2+} diffusion conditions towards the bulk solution. We presumed that the Fe^{2+} diffusion during aging
338 is possible because of the high Fe^{2+} concentration gradient between the area of local anodic sites and
339 the bulk solution. To sum up, in the absence of a strong oxidant (i.e., contaminant), water can
340 eventually penetrate weak points in the FeS_m shell (i.e., access Fe^0 sites) to form anodic and cathodic
341 sites. However, for gradual Fe^0 core depletion to occur as observed here, and without clear indications
342 for corrosion products inhibiting the process, these reactions (Eq. 1-2) must occur at different weak
343 sites, mimicking a galvanic-like corrosion condition. Noteworthy, this mechanism holds true if the rate
344 of water reduction at FeS_m sites is low. We believe this is true because numerous studies have shown
345 that the presence of FeS_m sites suppressed H_2 formation in comparison to non-sulfidized ZVI.[4,6,34,35]

346 This is further corroborated by our own results where we see little if any corrosion within the first 10
347 days of aging in anoxic artificial groundwater.

348 A last point to discuss in relation to corrosion mechanism is the observed heterogeneity in Fe^0 core
349 content after 180 days of aging. Seeing almost completely "hollow" particles (Fig. 4b), along with
350 particles that retained parts or most of their initial Fe^0 core (Fig. 4d), suggest that the FeS_m shell "weak"
351 points (i.e., the number of shell structural discontinuities) varies amongst particles. As such, S-nZVI
352 that exhibit shells with a high number of "weak" points likely corrode first and faster, while S-nZVI
353 with lower shell heterogeneities are able to preserve their Fe^0 core thereby sustaining their reactivity
354 with TCE for prolonged periods. Presumably, this could explain why Fe^0 corrosion and k_{obs} stabilized at
355 the latter stage in groundwater aging experiments (i.e., 60-120 days, Figure 6) and why k_{obs} almost
356 plateaued following the 4th TCE amendment in the re-spiking experiment (Figure S9).

357 In the case when TCE is consistently present, analogous to our re-spiking experiments, the general
358 assumption is that the cathodic reaction (i.e., TCE reduction) occurs at FeS_m sites while Fe^0 sites
359 become oxidized. This is heavily supported by reactivity studies that show enhanced TCE degradation
360 in the presence of an FeS_m shell.[4,6] Moreover, it is argued that the FeS_m shell facilitates TCE sorption
361 and reduction due to its enhanced hydrophobic and electron conductive properties.[6,24,30,35] Our data
362 support these assumptions. We reveal that the particle surface is often dominated by (001) FeS_m plane
363 features, which are considered to be the most hydrophobic and conductive in comparison to other
364 FeS_m planes.[18,19,36–38] The reason for such conductivity stems from the similarity in Fe-Fe interatomic
365 distance between FeS_m and Fe^0 (body centered cubic),[18,39,40] which is also evident in our d-PDF data
366 (Figure 1c). Moreover, our re-spiking experiments clearly showed that it is the Fe^0 core that gets
367 oxidized, while the shell structure seems to remain intact, with no other FeS phases detected. This
368 suggests that the core-shell architecture is robust and that in the presence of continued exposure to
369 target contaminants, electron efficiency is achieved.[28]

370

371 **4. Environmental Implications**

372 Our data clearly showed that the longevity of S-nZVI is heavily dependent on the architecture and
373 homogeneity of the FeS_m shell structure. Overall, prolonged and sustained S-nZVI reactivity is enabled
374 by the persistent FeS_m shell providing hydrophobic and electron conductive sites for TCE reduction
375 (cathodic reaction), while exhibiting a number of defect sites that facilitate the continuous but
376 controlled Fe^0 core oxidation (anodic reaction). The spatial separation of anodic and cathodic sites in
377 both reactivity scenarios (i.e., after aging with and without TCE) is argued to be key to maintain S-nZVI
378 reactivity as it allows for corrosion products (i.e. GR_{CO3}, WR) to form external to S-nZVI surfaces,
379 thereby limiting surface passivation. A point to consider, however, while a perfectly homogeneous
380 FeS_m shell with minimal defects would seem to enable high S-nZVI longevity in groundwater settings
381 (i.e., limited corrosion by water), it may also decrease the sufficient "accessible" anodic sites (i.e., Fe^0
382 oxidation sites), which ultimately increase the risk of surface passivation. Furthermore, while TCE can
383 be quickly reduced at FeS_m sites, other chlorinated ethenes such as cis-DCE, which often co-exist with
384 TCE in contaminant plumes, require Fe^0 sites for reduction.[8] Thus, a balance between FeS_m shell
385 features and target contaminant should also be assessed to realize an optimal *in*-situ remediation.

386 The results shown here are a product of idealized and simplified scenarios. Therefore, other factors
387 should also be considered such as specific groundwater chemistries (i.e., ion effects, pH conditions)
388 and presence of microbiomes that participate in sulfur and iron cycling;[41,42] all of which may impact
389 the stability of FeS_m or influence the corrosion rate of Fe^0 in S-nZVI. Additionally, consideration should
390 also be given to understand the controls of S-nZVI nanostructure during synthesis to further tailor its
391 application to specific groundwater contaminants and in various types of subsurface environments.

392 **Acknowledgements**

393 The authors thanks Olaf Borkiewicz and Kevin A. Beyer for support with X-ray total scattering
394 measurements at APS beamline 11 ID-B, Argonne, USA. We also thank Richard Wirth for the assistance
395 in TEM experimental set-up. This research was funded by Metal-Aid Innovative Training Network (ITN),

supported by a grant from the European Commission's Marie Skłowdowska Curie Actions program under project number 675219. LGB and HMF also acknowledge financial support by the Helmholtz Recruiting Initiative (Award No. I-044-16-01). Part of the data was acquired at Advanced Photon Source, a U.S. Department of Energy (DOE) Office of Science User Facility operated for the DOE Office of Science by Argonne National Laboratory under contract no. DE-AC02-06CH11357. Support for travel to the synchrotron facility came from the Danish Council for Independent Research (via DANSCATT).

References

1 E. C. Butler and K. F. Hayes, *Environ. Sci. Technol.*, 2001, **35**, 3884–3891.

2 D. Fan, R. P. Anitori, B. M. Tebo, P. G. Tratnyek, J. S. L. Pacheco, R. K. Kukkadapu, M. H. Engelhard, M. E. Bowden, L. Kovarik and B. W. Arey, *Environ. Sci. Technol.*, 2013, **47**, 5302–5310.

3 E. J. Kim, J. H. Kim, A. M. Azad and Y. S. Chang, *ACS Appl. Mater. Interfaces*, 2011, **3**, 1457–1462.

4 S. R. C. Rajajayavel and S. Ghoshal, *Water Res.*, 2015, **78**, 144–153.

5 J. Xu, Y. Wang, C. Weng, W. Bai, Y. Jiao, R. Kaegi and G. V Lowry, *Environ. Sci. Technol.*, 2019, **53**, 5936–5945.

6 D. Fan, G. O'Brien Johnson, P. G. Tratnyek and R. L. Johnson, *Environ. Sci. Technol.*, 2016, **50**, 9558–9565.

7 D. Fan, Y. Lan, P. G. Tratnyek, R. L. Johnson, J. Filip, D. M. O'Carroll, A. Nunez Garcia and A. Agrawal, *Environ. Sci. Technol.*, 2017, **51**, 13070–13085.

8 M. Mangayayam, K. Dideriksen, M. Ceccato and D. J. Tobler, *Environ. Sci. Technol.*, 2019, **53**, 4389–4396.

9 A. Liu, J. Liu, J. Han and W. X. Zhang, *J. Hazard. Mater.*, 2017, **322**, 129–135.

10 E. J. Smith, W. Davison and J. Hamilton-Taylor, *Water Res.*, 2002, **36**, 1286–1296.

11 D. J. Tobler, J. D. Rodriguez-Blanco, K. Dideriksen, N. Bovet, K. K. Sand and S. L. S. Stipp, *Adv. Funct. Mater.*, 2015, **25**, 3081–3090.

12 R. W. Wyckoff, *Crystal Structures Vol 1*, Interscience Publishers, New York, 1948.

13 D. Csákberényi-malasics, J. D. Rodriguez-blanco, V. Kovács, A. Re, L. G. Benning and M. Pósfai, *Chem. Geol.*, 2012, **294**–**295**, 249–258.

14 M. Wolthers, S. Van der Gaast and D. Rickard, *Am. Mineral.*, 2003, **88**, 2007–2015.

15 W. Li, R. Harrington, Y. Tang, J. D. Kubicki, M. Aryanpour, R. J. Reeder, J. B. Parise and B. L. Phillips, *Environ. Sci. Technol.*, 2011, **45**, 9687–9692.

16 R. Harrington, D. B. Hausner, N. Bhandari, D. R. Strongin, K. W. Chapman, P. J. Chupas, D. S. Middlemiss, C. P. Grey and J. B. Parise, *Inorg. Chem.*, 2010, **49**, 325–330.

17 D. J. Vaughan and M. S. Ridout, *J. Inorg. Nucl. Chem.*, 1971, **33**, 741–746.

18 D. Rickard and G. W. Luther, *Chem. Rev.*, 2007, **107**, 514–562.

19 A. Devey, R. Grau-Crespo and N. De Leeuw, *J. Phys. Chem. B*, 2008, **112**, 10960–10967.

20 S. A. T. Redfern and D. J. Vaughan, 1972, **59**, 677–683.

21 F. M. Michel, S. M. Antao, P. J. Chupas, P. L. Lee and J. B. Parise, 2005, 6246–6255.

22 A. Matamoros-Veloza, O. Cespedes, B. R. G. Johnson, T. M. Stawski, U. Terranova, N. H. de Leeuw and L. G. Benning, *Nat. Commun.*, 2018, **9**, 1–7.

23 A. Matamoros-Veloza, T. M. Stawski and L. G. Benning, *Cryst. Growth Des.*, 2018, **18**, 6757–6764.

24 S. Song, Y. Su, A. S. Adeleye, Y. Zhang and X. Zhou, *Appl. Catal. B Environ.*, 2017, **201**, 211–

220.

25 S. Boursiquot, M. Mullet, M. Abdelmoula, J.-M. Génin and J.-J. Ehrhardt, *Phys. Chem. Miner.*, 2001, **28**, 600–611.

26 J. B. Harrison and V. E. Berkheiser, *Clays Clay Miner.*, 1982, **30**, 97–102.

27 *Hyperfine Interact.*, 1994, **90**, 395–400.

28 F. He, Z. Li, S. Shi, W. Xu, H. Sheng, Y. Gu, Y. Jiang and B. Xi, *Environ. Sci. Technol.*, 2018, **52**, 8627–8637.

29 L. G. Benning, R. T. Wilkin and H. L. Barnes, *Chem. Geol.*, 1999, **167**, 25–51.

30 D. Li, Z. Mao, Y. Zhong, W. Huang, Y. Wu and P. Peng, *Water Res.*, 2016, **103**, 1–9.

31 H. Dong, C. Zhang, J. Deng, Z. Jiang, L. Zhang, Y. Cheng, K. Hou, L. Tang and G. Zeng, *Water Res.*, 2018, **135**, 1–10.

32 F. A. Weber, A. Voegelin, R. Kaegi and R. Kretzschmar, *Nat. Geosci.*, 2009, **2**, 267–271.

33 A. Cabot, V. F. Puntes, E. Shevchenko, Y. Yin, L. Balcells, M. A. Marcus, S. M. Hughes and A. P. Alivisatos, *J. Am. Chem. Soc.*, 2007, **129**, 10358–10360.

34 J. Oudar, *Catal. Rev. Sci. Eng.*, 1980, **22**, 171–195.

35 Y. Han and W. Yan, *Environ. Sci. Technol.*, 2016, **50**, 12992–13001.

36 N. Y. Dzade, A. Roldan and N. H. De Leeuw, *J. Phys. Chem. C*, 2016, **120**, 21441–21450.

37 N. Y. Dzade, A. Roldan and N. H. De Leeuw, *J. Chem. Phys.*, , DOI:10.1063/1.4822040.

38 N. Y. Dzade, A. Roldan and N. H. De Leeuw, *J. Chem. Phys.*, , DOI:10.1063/1.4929470.

39 M. Wolthers, L. Charlet, P. van Der Linde, D. Rickard and C. van Der Weijden, *Geochim. Cosmochim. Acta*, 2005, **69**, 3469–3481.

40 W. M. Skinner, H. W. Nesbitt and A. R. Pratt, *Geochim. Cosmochim. Acta*, 2004, **68**, 2259–2263.

41 T. M. Flynn, E. J. O. Loughlin, B. Mishra, T. J. Dichristina and K. M. Kemner, *Science (80-.).*, 2014, **344**, 1039–1043.

42 K. P. Nevin and D. R. Lovley, *Environ. Sci. Technol.*, 2000, **34**, 2472–2478.